

The long-term evolution of neutron star merger remnants – II. Radioactively powered transients

Doron Grossman¹, Oleg Korobkin², Stephan Rosswog² and Tsvi Piran¹

¹*Racah Institute of Physics, The Hebrew University, Jerusalem 91904, Israel*

²*Astronomy and Oskar Klein Centre, Stockholm University, AlbaNova, SE-10691 Stockholm, Sweden*

20 January 2014

ABSTRACT

We use 3D hydrodynamic simulations of the long-term evolution of neutron star merger ejecta to predict the light curves of electromagnetic transients that are powered by the decay of freshly produced r-process nuclei. For the dynamic ejecta that are launched by tidal and hydrodynamic interaction, we adopt grey opacities of $10 \text{ cm}^2/\text{g}$, as suggested by recent studies. For our reference case of a $1.3 - 1.4 M_{\odot}$ merger, we find a broad IR peak 2-4 d after the merger. The peak luminosity is $\approx 2 \times 10^{40} \text{ erg/s}$ for an average orientation, but increased by up to a factor of 4 for more favourable binary parameters and viewing angles. These signals are rather weak and hardly detectable within the large error box ($\sim 100 \text{ deg}^2$) of a gravitational wave trigger. A second electromagnetic transient results from neutrino-driven winds. These winds produce ‘weak’ r-process material with $50 < A < 130$ and abundance patterns that vary substantially between different merger cases. For an adopted opacity of $1 \text{ cm}^2/\text{g}$, the resulting transients peak in the UV/optical about 6 h after the merger with a luminosity of $\approx 10^{41} \text{ erg/s}$ (for a wind of $0.01 M_{\odot}$). These signals are marginally detectable in deep follow-up searches (e.g. using Hypersuprime camera on Subaru). A subsequent detection of the weaker but longer lasting IR signal would allow an identification of the merger event. We briefly discuss the implications of our results to the recent detection of an nIR transient accompanying GRB 130603B.

Key words: transients, gamma-ray bursts, infrared sources, nuclear reactions, neutron stars

1 INTRODUCTION

The merger of two neutron stars (ns^2), or, alternatively, of an ns with a stellar-mass black hole (nsbh), plays a key role for several astrophysical questions. Such mergers are in the main focus of current efforts towards direct gravitational wave (GW) detections, they are thought to be the ‘engines’ of short gamma-ray bursts (sGRBs; see Piran 2004; Lee & Ramirez-Ruiz 2007; Nakar 2007, for reviews) and they may produce the heaviest elements in the Universe (Lattimer & Schramm 1974; Lattimer et al. 1977; Eichler et al. 1989; Freiburghaus et al. 1999). Until recently, each of these topics has been mostly studied in its own right, and currently much effort is invested in integrating the different facets of the topic into a coherent multi-messenger picture (Bloom et al. 2009; Phinney 2009; Metzger & Berger 2012; Bartos, Brady & Márka 2013; Kasliwal & Nissanke 2013; Kelley, Mandel & Ramirez-Ruiz 2012; Nissanke, Kasliwal & Georgieva 2013; Rosswog, Piran & Nakar 2013; Piran, Nakar & Rosswog 2013)

By the end of this decade the second generation of ground-

based GW detectors is expected to be running at their intended design sensitivities (Harry & LIGO Scientific Collaboration 2010; Accadia et al. 2011; Somiya 2012). The main target of these detectors is the discovery of the chirping GW signals from ns^2 or nsbh mergers. The expected detection horizons are a few hundred Mpc for ns^2 mergers and about a Gpc for nsbh mergers (445/927 Mpc are adopted by the LIGO-Virgo collaboration as canonical values; Abadie et al. 2010).

It had been realized early on that an electromagnetic (EM) transient coincident with the GW signal could deliver crucial complementary information (Kochanek & Piran 1993; Hughes & Holz 2003; Dalal et al. 2006; Arun et al. 2009). A spatial and temporal coincidence between a GW and an expected EM signal would enhance the confidence in a GW detection and thereby effectively enhance the sensitivity of existing GW detector facilities. GW detections can provide the parameters of the merging system such as the individual masses or the orbital inclination, but with sky localizations of tens of degrees they leave us essentially blind with respect to the astronomical environment of a merger. Additional EM

transients can complement the picture by, for example, delivering accurate source localizations or redshifts and they can therefore provide independent pieces of evidence for the nature of the observed event. Moreover, even before the detector facilities are fully upgraded, EM transients could improve the poorly constrained merger rates.

sGRBs have been long recognized (Eichler et al. 1989) as possible EM counterparts of compact binary mergers. Circumstantial evidence for this association arises from various lines of argument. For example, the overall sGRB rate (Guetta & Piran 2006; Nakar et al. 2006; Guetta & Stella 2009; Coward et al. 2012) is comparable to the estimates for binary neutron stars (Narayan et al. 1991; Phinney 1991; Kalogera et al. 2004a,b; Abadie et al. 2010) and the redshift distribution of sGRBs is consistent with sources that are delayed with respect to the star formation rate (Guetta & Piran 2006; Nakar et al. 2006; Nakar 2007). Further evidence comes from the location of some sGRBs within elliptical galaxies which harbor very little star formation and from the location of sGRBs with respect to their host galaxies (Berger 2009, 2010; Fong et al. 2010, 2013). However, sGRBs are most likely beamed, both theoretical and observational studies point to opening angles roughly around 5° (Rosswog & Ramirez-Ruiz 2003; Aloy et al. 2005; Fong et al. 2012), but with large uncertainties. Most likely the beaming factor is large and in most cases the sGRB will be undetectable since it points away from us. In fact, since *Swift* has begun operating in 2004, no sGRB has been detected with a redshift below $z \approx 0.12$ (Rowlinson et al. 2010), while the envisaged horizons of the advanced detector facilities are $\approx 0.05/0.1$ for ns^2 and nsbh mergers.

‘Macronovae’¹ are more isotropic transients that are powered by freshly synthesized radioactive isotopes and therefore are closely related to cosmic nucleosynthesis. After it had been realized that ns mergers eject $\sim 0.01M_\odot$ (Rosswog et al. 1998, 1999) and that the ejecta consist essentially entirely of heavy ($A > 130$) r-process matter (Freiburghaus et al. 1999), Li & Paczyński (1998) addressed the question how an ns merger would look electromagnetically. In their first approach, they modelled the ejecta as a uniformly expanding sphere with a fixed opacity of $\kappa = 0.2 \text{ cm}^2/\text{g}$ and assumed that a fraction f of the rest mass would be channelled into radioactive heating. Subsequently much effort has been invested in refining macronova models and in further understanding their properties (Kulkarni 2005; Rosswog 2005; Metzger et al. 2010; Goriely et al. 2011; Roberts et al. 2011; Bauswein et al. 2013; Piran et al. 2013; Rosswog et al. 2013). All of these studies share the use of opacities that are characteristic for the line expansion opacities of iron group elements. Kasen et al. (2013), however, recently pointed out that the opacities of compact binary merger ejecta are likely dominated by elements with half-filled f-shells such as lanthanides and actinides which have extremely large opacities even if their mass fraction is as low as 1 per cent. Based on detailed atomic structure calculations they concluded that average opacities may be around $10 \text{ cm}^2/\text{g}$ (rather than the previously used much lower values) and this would lead to weaker, later and redder emission (Barnes & Kasen 2013).

¹ This term has been introduced to the literature by Kulkarni (2005), other authors prefer ‘kilonova’ (Metzger et al. 2010).

Tanaka & Hotokezaka (2013) followed a complementary approach by using a new line list for r-process elements based on the VALD data base (Kupka et al. 2000) and applied it in radiative transfer calculations to a 2D, axisymmetric ejecta model that is based on the merger simulations of Hotokezaka et al. (2013). They also favour opacity values around $10 \text{ cm}^2/\text{g}$.

In this study we make use of the 3D ejecta geometry as calculated in hydrodynamic simulations that include the heating from radioactive decays. The overall hydrodynamic evolution with a particular focus on the effect of the r-process heating is discussed in a companion paper, thereafter referred to as ‘Paper I’ (Rosswog et al. 2013). Implications of these calculations for light curves of accompanying radio flares (Nakar & Piran 2011; Piran et al. 2013) will be discussed elsewhere. The rest of this paper is structured as follows. In Sec. 2, we describe our hydrodynamics results and in Sec. 3, we briefly review the nucleosynthesis in the ejecta. We discuss the nuclear energy release and the expected opacities, mainly based on the recent work by Kasen et al. (2013). Again for some parts we will refer to paper I for more details. In Sec. 4, we discuss in detail the radioactive transients that are expected from the dynamic ejecta. Our results are based on the true matter distribution, but we also examine the accuracy of various semi-analytic approaches. In Sec. 5, we discuss a second radioactive transient that results from neutrino-driven winds. This radioactive material is also produced in an r-process, though different from the one that occurs inside the dynamic ejecta. While the latter is a ‘strong r-process’ that very robustly produces in each event the same abundance pattern of very heavy elements ($A > 130$), the former is a ‘weak’ r-process whose abundances vary depending on the detailed neutrino luminosities and which produces less heavy nuclei in a range $50 \lesssim A \lesssim 130$. This has implications for both the radioactive half-lives and the opacities and therefore the properties of this second radioactive transient differ from the more commonly considered radioactive transient that arises from the dynamic ejecta. In Sec. 6, we discuss the detectability of these transients and we summarize and conclude in Sec. 7, where we also briefly discuss the implications of our results to the recent detection of an nIR transient accompanying GRB 130603B (Tanvir et al. 2013; Berger et al. 2013).

2 HYDRODYNAMICS

We begin by briefly summarizing our hydrodynamic simulations, for more details we refer to Paper I and the references therein. The simulations of this paper begin from the final configurations of calculations presented in Rosswog et al. (2013) and Rosswog (2013). These simulations were performed with a 3D smoothed particle hydrodynamic (SPH) code that has been described in previous publications (Rosswog et al. 2000; Rosswog & Davies 2002; Rosswog & Liebendörfer 2003; Rosswog & Price 2007). For reviews of the SPH method, we refer to Monaghan (2005), Rosswog (2009) and Springel (2010). The subsequent long-term evolution is performed with a variant of the above code that uses different units and physics ingredients (Rosswog et al. 2008). In particular, we switch from the Shen equation of state (EOS; Shen et al. 1998a,b) to the Helmholtz EOS (Timmes

& Swesty 2000), and when we hit the lower input limits of the latter, we smoothly switch over to a Maxwell–Boltzmann gas plus radiation. We systematically account for the heating from radioactive decays by employing fit formulae for the nuclear energy generation rate, ϵ_{nuc} , and the average nucleon and proton numbers which are needed to call the Helmholtz EOS. For the explicit forms of the fit formulae, we refer to appendix A of Paper I.

To follow the long-term evolution of the dynamically ejected matter, we cut out the central object and accretion torus, typically at a radius of $R_{\text{cut}} = 300$ km, and replace the corresponding matter with a point mass. We follow the evolution of the ejecta up to 100 years for a number of exemplary systems: a) an equal mass merger with $2 \times 1.4 M_{\odot}$, b) a merger with a slight asymmetry, 1.4 and $1.3 M_{\odot}$, c) a merger of a 1.6–1.2 M_{\odot} system and finally d) the merger of a 1.8 M_{\odot} ns with a 1.2 M_{\odot} ns. The physical parameters of these simulations are summarized in Table 1.

In Fig. 1, we show the density distribution in the orbital plane at $t = 1$ d after the merger which is characteristic for the peak time of macronovae. In the equal-mass case (top left), the remnant is symmetric with two tidal tails, for the other cases only one tidal emerges which becomes more pronounced with increasing deviations of the mass ratio from unity.

Fig. 2 shows snapshots of the radial and polar angle mass distributions at different epochs. Mass accelerates due to radioactive heating, but settles quickly to a homologous expansion. While there is significant acceleration from the moment of merger until after the neutron freeze-out (dotted and dashed lines in Fig. 2), from there on distributions change only slightly. The cases of 1.6–1.2 and 1.8–1.2 M_{\odot} have much broader initial radial distributions, while at later times the distribution shrinks towards the centre. This does not mean, however, that the mass is decelerating, because the radial distributions in Fig. 2a are calculated with respect to the density maximum. If the location of the latter changes with time, so does the distribution. In both merger cases mentioned above the tidal tails are initially highly non-spherical with a compact dense core and an extended tail. As the merger remnant expands and puffs up due to radioactive heating, the density maximum moves closer to the geometric centre and the distribution becomes more centrally condensed.

Fig. 2b shows the amount of mass contained in a cone with an opening angle θ with respect to the initial binary rotation axis. This quantity is important since it determines whether the neutrino-driven wind that we discuss in §5 can escape along the rotation axis or not. This figure shows that only a small amount of mass is contained in the polar region. This implies that a neutrino-driven wind that is produced shortly after the merger can likely escape without a significant interaction with the dynamic ejecta.

As discussed in Paper I, all of our models show homologous expansion with the degree of homology up to 0.01 per cent at the time period which is relevant for the macronova calculations (1 d).

Table 1. Overview of the performed simulations; all neutron stars have zero initial spin. N_{SPH} is the number of SPH particles in the initial ns² simulation, and t_{end} is the time when the initial ns² merger simulation is stopped; the hydrodynamic evolution of the ejecta is subsequently followed up to a time of 100 years. $m_{\text{ej},-2}$ is the ejected mass in units of $10^{-2} M_{\odot}$, and $v_{1/2}$ is the median velocity in the final radial mass-velocity profile (see Fig. 2a).

Run ($m_1 - m_2$)	N_{SPH}	t_{end} (ms)	$m_{\text{ej},-2}$	$v_{1/2}(c)$
A (1.4 – 1.4)	1.0×10^6	13.4	1.3	0.095
B (1.3 – 1.4)	2.7×10^6	20.3	1.4	0.086
C (1.6 – 1.2)	1.0×10^6	14.8	3.3	0.119
D (1.8 – 1.2)	1.0×10^6	21.4	3.4	0.121

3 NUCLEOSYNTHESIS AND OPACITIES

The macronova transients that we are interested in are caused by radioactive matter that is ejected into space during a compact binary merger. There are at least three ejection channels for neutron-rich matter in a compact binary merger: a) the dynamic ejecta that are launched by hydrodynamic interaction and/or gravitational torques (Rosswog et al. 1999; Bauswein et al. 2013; Hotokezaka et al. 2013; Rosswog 2013), b) neutrino-driven winds from the remnant (Ruffert et al. 1997; Rosswog & Ramirez-Ruiz 2002, 2003; Rosswog et al. 2003; Surman et al. 2008; Dessart et al. 2009; Caballero et al. 2012; Wanajo & Janka 2012) and c) the final disintegration of accretion discs that occurs when viscous dissipation and the recombination of nucleons into light nuclei conspire to unbind a substantial fraction of the initial accretion disc (Lee & Ramirez-Ruiz 2007; Beloborodov 2008; Metzger et al. 2008; Lee et al. 2009; Metzger et al. 2009; Fernández & Metzger 2013).

Each of these channels may eject matter with different properties which impacts on both nucleosynthesis and possible radioactive transients. So far, the dynamic ejecta have received most attention although the other channels may have interesting consequences as well. The dynamic ejecta are launched essentially immediately at first contact, even before the neutrino emission has reached substantial values. Therefore, the ejecta electron fraction is very close to the initial cold β -equilibrium value of around $Y_e = 0.03$ (Korobkin et al. 2012). Under these conditions matter undergoes a ‘strong’ r-process and produces very heavy nuclei ($A > 130$) with a robust abundance pattern that is independent of the parameters of the merging compact binary (Korobkin et al. 2012; Bauswein et al. 2013, Paper I).

The neutrino-driven wind case is different in several respects. Here, matter is not ejected immediately but instead exposed to neutrino fluxes for a much longer time and it is only gradually accelerated by capturing (anti-)neutrinos in β -processes. Therefore, it is the relative neutrino luminosities and energies that determine the final Y_e values, like in the case of proto-neutron stars (Qian & Woosley 1996). The differences in the neutrino properties of our four considered cases, see table 1 in Paper I, therefore lead to a relatively large spread in the asymptotic wind electron fractions: 0.28 for run A, 0.30 for run B, 0.36 for run C and 0.40 for run D. In this regime, the nucleosynthesis is actually rather sensi-

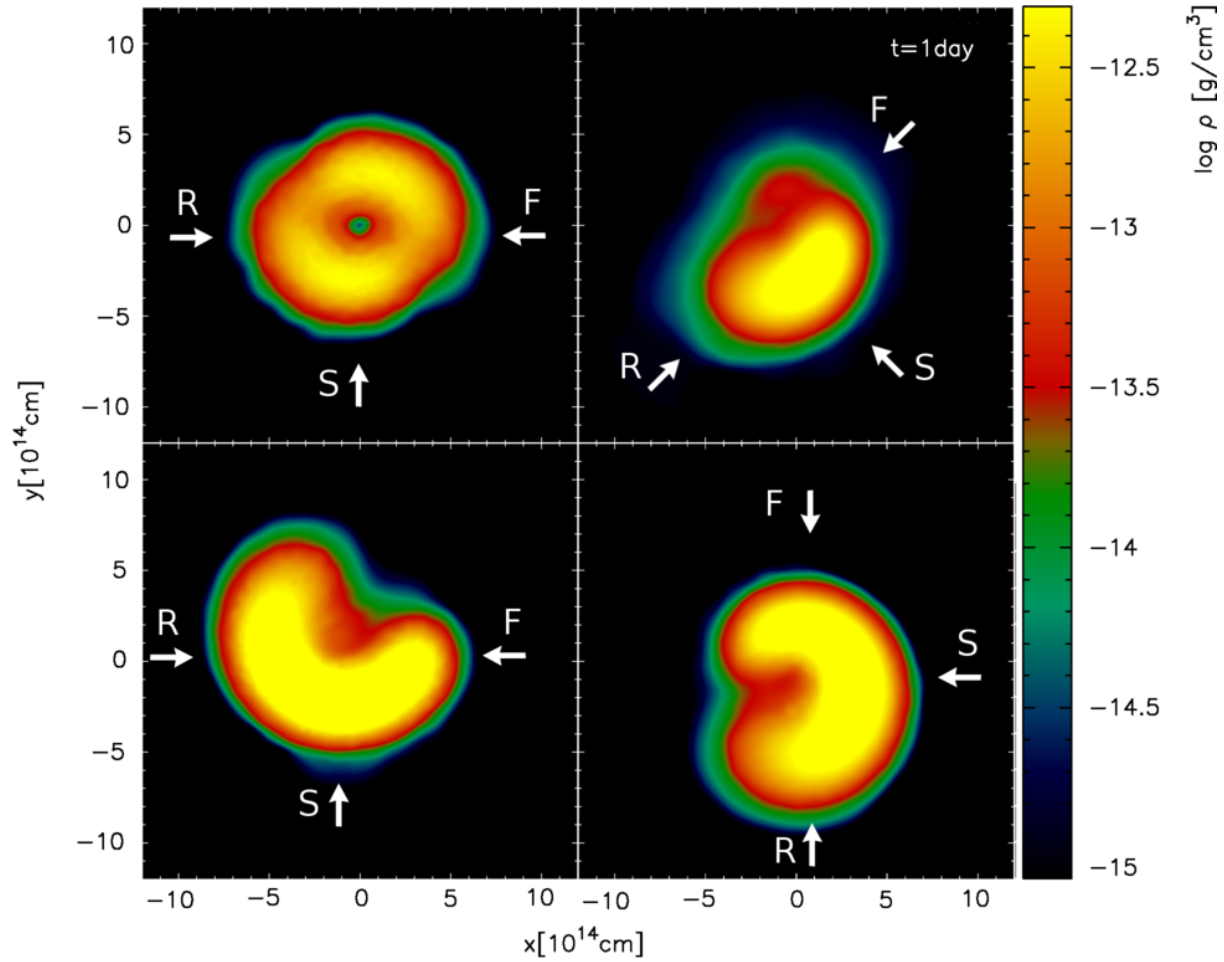


Figure 1. Density in the orbital plane at one day after the merger, for the different merger cases. Top left: $1.4\text{--}1.4 M_{\odot}$, top-right: $1.3\text{--}1.4 M_{\odot}$, bottom-left: $1.6\text{--}1.2 M_{\odot}$ and bottom right: $1.8\text{--}1.2 M_{\odot}$. The arrows indicate three different viewing angles that are referred to in later figures, and the fourth ‘top’ view direction (not shown) is always perpendicular to the orbital plane.

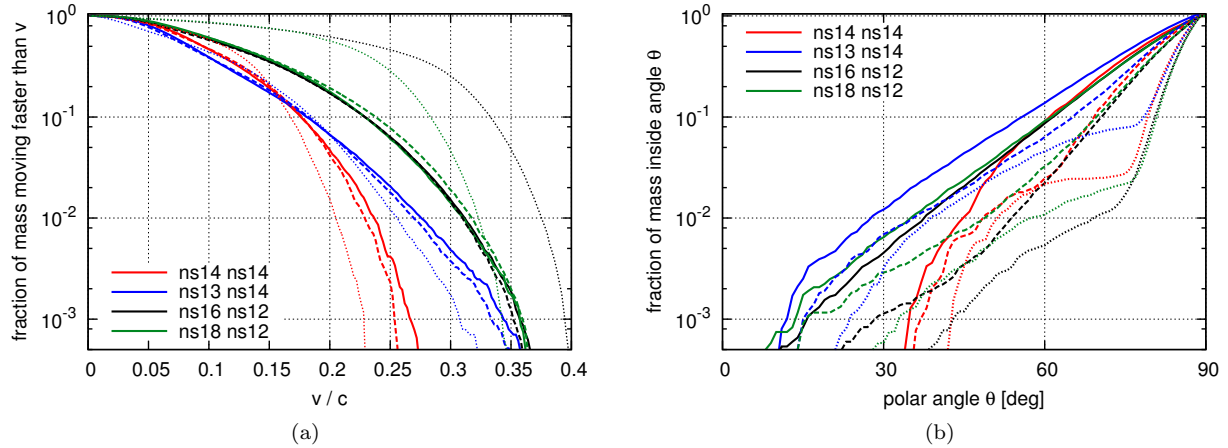


Figure 2. Snapshots of radial and angular mass distributions for different merger cases at different times. Shown are initial distributions right after the merger (dotted lines), distributions at 2 s (dashed lines) and at late time (solid lines): (a) spherical mass distribution, mass with velocity larger than v as a function of v . One can clearly see the acceleration of the matter due to the radioactive decay. The distribution settles to a simple homologous expansion after a few hours. (b) Mass within angle smaller than θ as a function of polar angle θ . This plot demonstrates that there is no significant mass in the polar region even after the remnant has puffed up due to radioactive heating. Thus, the dynamic ejecta leave a rather empty wide funnel along the rotation axis in which the neutrino-driven wind can escape.

tive to the exact value of the electron fraction; therefore, the four merger cases produce a substantial spread in the resulting abundance patterns. In all cases, our model, see Paper I for more details, produces abundance distributions in the range $50 \lesssim A \lesssim 130$ that show substantial variations from case to case due to the different initial Y_e . Our wind model is for sure very simple; it is mainly meant to illustrate some basic points and qualitative features: a) a neutrino-driven wind produces also r-process, though only lower mass, ‘weak’ r-process contributions and b) it can plausibly produce another transient EM event that is powered by radioactivity, though not ^{56}Ni .

For the third channel, the dissolution of accretion discs on viscous time-scales, recent models (Fernández & Metzger 2013) find that also ~ 10 per cent could become unbound with electron fractions of ~ 0.2 . To our knowledge, no detailed nucleosynthesis results exist yet for this material, although Fernández & Metzger (2013) argue for this outflow channel to also produce heavy r-process elements (based on the parametrized study of Hoffman et al. 1997). In the following, we will focus entirely on the former two channels.

The spread in the abundance patterns also translates to the opacities. Kasen et al. (2013) suggest that the elements with half-filled f-shells such as lanthanides and actinides should have very high opacities around $10 \text{ cm}^2/\text{g}$, consistent with the conclusions of Tanaka & Hotokezaka (2013). We therefore adopt this value in our study. For the wind material, we adopt a lower value, $\kappa = 1 \text{ cm}^2/\text{g}$. This needs admittedly further study in the future, but we consider this justified at the current stage since our model is mainly to illustrate qualitatively the plausibility of a second transient. It is worthwhile pointing out, however, that for these grey opacities our results satisfy simple scaling laws and the results apply, after this scaling, to any system in which the opacity is frequency independent.

We had recently found (Korobkin et al. 2012) that the nuclear energy generation rate is relatively independent of details and has a simple temporal dependence: it is constant within roughly the first second and subsequently decays according to a power law $\propto t^{-\alpha}$, where $\alpha = 1.3$, similar to the results found by other groups (Metzger et al. 2010; Gorieli et al. 2011; Roberts et al. 2011). The energy generation and the average nucleon and proton number that are needed to call the EOS can be easily fit as a function of time and they are included into the hydrodynamic simulation via fit formulae; the explicit expressions are given in appendix A of Paper I.

All the nucleosynthesis results that we are quoting here and in Paper I have been obtained with the nuclear reaction network of Winteler (Winteler 2012; Winteler et al. 2012) which is an update of the BasNet network (Thielemann et al. 2011).

4 THE LIGHT CURVES

We did not carry out detailed radiation transfer simulations, instead we use simple approximations, discussed below, that capture the main characteristics of the radiation from the expanding remnant. The basic idea is that photons can escape in a dynamical time from the region $R > R_{\text{diff}}$, where R_{diff} is the radius from which the diffusion time, t_{diff} , equals the dy-

namical time, $t_{\text{dyn}} = r/v = t$. These photons diffuse out in the optically thick regime until they reach the photosphere at $\tau = 2/3$. The photons escape from the photosphere with a quasi-thermal, possibly blackbody but basically unknown spectrum. The details of this spectrum depend very strongly on unknown features of the opacity. Emission generated at the region $\tau < 2/3$ escapes most likely at high energies and with an unknown spectrum. We neglect this radiation in our calculations as it is most unlikely that it will be at the IR–optical range that we consider here. Indeed, all X-rays and γ -radiation produced directly in radioactive decays freely escape, while high-energy electrons need several scattering events before they could induce bound–bound transitions in optical or IR. But in the low-density transparent medium, they are not able to efficiently thermalize, so their energy will be ultimately lost to expansion. The luminosity of this optically thin component is shown as blue dotted line in Fig. 3.

We begin in §4.1 with simple analytic estimates of the escaping emission and continue in §4.2 with a detailed description of how we numerically calculate the radiation from the simulation results. In §4.3, we describe our results from the 3D matter distribution.

4.1 Analytic estimates

Before considering the numerical solutions we consider a few analytic approximations. The basic idea behind these approximations is that the radiation diffuses out from the region in which $t_{\text{diff}} \leq t_{\text{dyn}}$, i.e. the diffusion time is less than or equal to the dynamical time. The latter evolves uniformly and therefore simply equals t . The approximations differ in the estimates of the diffusion time.

We consider a spherical homologous system and define $m(v)$, the mass with velocity larger than v , which is shown in Fig. 2a. Since the system is highly homologous, this mass is located further out relative to the mass that is moving at lower velocities. The maximal velocity is denoted by v_{max} . The simplest and most commonly used approximation estimates the diffusion time as (e.g. Piran et al. (2013))

$$t_{\text{diff}} = \frac{\tau(v_{\text{max}} - v)t}{c} = \frac{m\kappa}{4\pi cvt}, \quad (1)$$

where the optical depth for the mass $m(v)$ is approximated as if this mass is distributed uniformly within a spherical layer of radius vt and thickness $(v_{\text{max}} - v)t$. This leads to an implicit equation for v :

$$\frac{m(v)}{v} = \frac{4\pi ct^2}{\kappa}. \quad (2)$$

In the first approximation, neglecting the fact that emission from an optically thin region ($\tau < 2/3$) escapes freely and not necessarily in the IR–optical or UV bands, we estimate the bolometric luminosity as:

$$L(t) = \dot{\epsilon}(t)m(v) = \dot{\epsilon}_0(t/t_0)^{-\alpha}m(v), \quad (3)$$

where t_0 denotes the onset of the power law decay ($\approx 1 \text{ s}$), and $\dot{\epsilon}_0$ is the heating rate at $t = t_0$. This approximation is commonly used to estimate the peak time, \tilde{t}_p , and peak bolometric luminosity, \tilde{L}_p :

$$\tilde{t}_p \approx \sqrt{\frac{\kappa m_{\text{ej}}}{4\pi c \bar{v}}} = 4.9 \text{ d} \left(\frac{\kappa_{10} m_{\text{ej},-2}}{\bar{v}_{-1}} \right)^{1/2}, \quad (4)$$

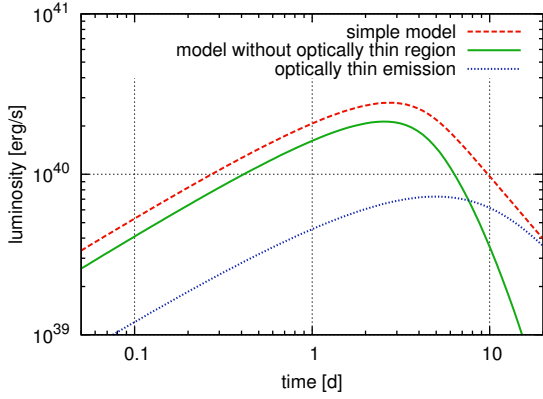


Figure 3. A comparison of the two approximate bolometric light curves given by two approximations for a fiducial profile having mass $m_{\text{ej}} = 0.01 M_{\odot}$ and density distribution $\rho(v) = \rho_0(1 - v^2/v_{\text{max}}^2)^3$, where $v_{\text{max}} = 0.35c$. The opacity is taken to be $\kappa = 10 \text{ cm}^2/\text{g}$. The simple model is described by a dashed line while the one with the optically thin region excluded is shown by a solid line. In the second approximation the effectively contributing radiating layer is smaller, leading to a slightly earlier and less luminous signal, which also has a much steeper decline. The blue dotted line shows the difference between the two, which corresponds to the power emitted in high-energy photons by the optically thin layer.

$$\begin{aligned} \tilde{L}_p &\approx \dot{\epsilon}_0 m_{\text{ej}} \left(\frac{\kappa m_{\text{ej}}}{4\pi c \bar{v} t_0^2} \right)^{-\alpha/2} = \\ &= 2.5 \times 10^{40} \frac{\text{erg}}{\text{s}} \left(\frac{\bar{v}_{-1}}{\kappa_{10}} \right)^{\alpha/2} m_{\text{ej},-2}^{1-\alpha/2}, \end{aligned} \quad (5)$$

where we defined $\kappa_{10} = (\kappa/10 \text{ cm}^2 \text{ g}^{-1})$, $m_{\text{ej},-2} = (m_{\text{ej}}/0.01 M_{\odot})$ and $\bar{v}_{-1} = (\bar{v}/0.1c)$. It is valid in the intermediate regime where radiation is produced by a significant fraction of the overall mass. If we are bold enough, we can even estimate the effective temperature. Assuming that the effective emitting area is of the order of $4\pi(vt)^2$, we obtain:

$$\begin{aligned} \tilde{T}_{\text{eff}} &\approx \left(\frac{\dot{\epsilon}_0 c}{\sigma_{\text{SB}}} \right)^{1/4} \left(\frac{m_{\text{ej}}}{4\pi c t_0} \right)^{-\alpha/8} \kappa^{-(\alpha+2)/8} \bar{v}_{-1}^{(\alpha-2)/8} \\ &= 2200 \text{ K } \kappa_{10}^{-(\alpha+2)/8} \bar{v}_{-1}^{(\alpha-2)/8} m_{\text{ej},-2}^{-\alpha/8}. \end{aligned} \quad (6)$$

In the second approximation we subtract the mass $m(v_{2/3})$ contained in the optically thin region:

$$L(t) = \dot{\epsilon}(t)(m(v) - m(v_{2/3})). \quad (7)$$

Fig. 3 depicts a comparison of the resulting bolometric light curves with both approximations for a mass distribution of the form $\rho(v) = \rho_0(1 - v^2/v_{\text{max}}^2)^3$. The simple model gives more or less the time at which that the whole system begins to emit and indeed shortly after this peak the emission settles to the late phase of $t^{-\alpha}$ decay. The model with the optically thin region excluded produces a luminosity which is smaller by about a factor of ~ 1.2 in the raising phase and a more rapid decline ($\propto t^{-(3+\alpha)}$), reflecting the fact that increasingly smaller fractions of emitted energy can be reprocessed into the UV, optical or infrared bands. The rest of the nuclear power produced in the optically thin region is lost to high-energy emission with an unknown spectrum. This power is shown in with the blue dotted line in Fig. 3.

4.2 Numerical treatment

For our numerical models we can produce light curves from a sequence of 3D snapshots of the expanding material. Alternatively, one can make use of the fact that the expansion is highly homologous for $t > 0.05 \text{ d}$, as shown in fig. 7 of Paper I. Therefore, most of the dynamical quantities can be obtained by a simple rescaling of a reference snapshot, taken for example at $t_0 = 1 \text{ d}$. Such a reference snapshot from run B ($1.3\text{--}1.4 M_{\odot}$) is shown in Fig. 4. One can distinguish three regions: the optically thick inner region, a ‘radiating volume’ between optical depths of τ_{diff} and $2/3$ and finally the transparent envelope with $\tau < 2/3$. In the inner region, the density is high and the photons are efficiently trapped inside the diffusion surface, defined by the condition that the photon diffusion time t_{diff} equals the dynamical time t_{dyn} . The former can be estimated as $t_{\text{diff}} = \zeta\tau/c$, where ζ is the length of the shortest photon ‘escape route’, normally following the negative gradient of the optical depth. The inner region does not contribute to the observed luminosity since the photons are trapped. The outer region likely does not contribute either, because the photons escape with large energies determined by the nuclear reactions.

We are therefore mainly interested in the region between the diffusion surface and the photosphere, with the latter defined by the condition $\tau = 2/3$. For general configurations, both of these surfaces can have non-trivial shape. Fig. 4a shows the contours of the photosphere and the diffusion surface at $t_0 = 1 \text{ d}$, along with the distribution of emissivity in the XY plane. We estimate the luminosity by integrating the emissivity over the ‘radiating volume’ between the photosphere and the diffusion surface (see Fig. 4a).

Due to the homologous expansion, we can use the particle velocities as time-independent coordinates. Then, the photosphere and the diffusion surface can be found as level surfaces of the optical depth $\tau(v)$ and $\tau(v)\zeta(v)$, specifically the surfaces defined by:

$$\tau(v) = \frac{2}{3} \left(\frac{t}{t_0} \right)^{-2}, \quad \tau(v)\zeta(v) = ct \left(\frac{t}{t_0} \right)^{-2}. \quad (8)$$

Fig. 4b shows the contours of $\tau(v)$ in velocity space for several successive times, and Fig. 5 shows these contours in 3D. The photosphere traverses a sequence of embedded level surfaces of $\tau(v)$, and so does the diffusion surface for the level surfaces of $\tau(v)\zeta(v)$. The combined effects of these two surfaces determine the luminosity and the effective temperature of the escaping emission.

We identify $\tau(\mathbf{r})$ and $\zeta(\mathbf{r})$ at $t_0 = 1 \text{ d}$ and perform the volume integration with properly rescaled quantities. With our assumption of constant opacity, the optical depth can be calculated by integrating $d\tau = \kappa\rho(z)dz$ along the path following the negative density gradient. Since the density is given in SPH representation, it is convenient to express $\tau(\mathbf{r})$ in the same way:

$$\tau(\mathbf{r}) = \sum_b \tau_b \frac{m_b}{\rho_b} W_b(\mathbf{r}), \quad (9)$$

where $W_b(\mathbf{r}) = W(|\mathbf{r} - \mathbf{r}_b|, h_b)$ is a smoothing kernel, h_b is the SPH particle smoothing length, and m_b and ρ_b are its mass and density. It suffices to calculate τ_b for every particle to properly approximate optical depth everywhere, and the similar SPH expansion is employed to represent $\zeta(\mathbf{r})$.

The total luminosity is calculated as:

$$L = \int_{\tau(\mathbf{r}) < ct/\zeta(\mathbf{r})} \dot{\epsilon}(t) \rho(\mathbf{r}) d^3 \mathbf{r} \approx \sum_{\substack{\tau_b < ct/\zeta_b \\ \tau_b > 2/3}} \dot{\epsilon}(t) m_b, \quad (10)$$

where the final sum runs over all particles with $\tau_b > 2/3$ and $\tau_b < ct/\zeta_b$.

To compute the luminosity radiated in a given direction, in principle one needs to solve complete radiative transfer equations. The energy originating deep in the bulk of the radiation layer will be transferred to the photosphere and spread over a finite region. To mimic this effect, we adopt the following simple approach. Because the luminous flux is more likely to stream in the direction of negative gradient of optical depth, the directional luminosity can be approximated by:

$$\frac{dL}{d\Omega}(\mathbf{k}) = \int_{\tau(\mathbf{r}) > 2/3, \mathbf{k} \cdot \mathbf{n} > 0}^{\tau(\mathbf{r}) < ct/\zeta(\mathbf{r})} \mathbf{k} \cdot \mathbf{n} \dot{\epsilon}(t) \rho(\mathbf{r}) d^3 \mathbf{r} \approx \quad (11)$$

$$\approx \sum_{\substack{\tau_b < ct/\zeta_b \\ \tau_b > 2/3, \mathbf{k} \cdot \mathbf{n} > 0}} \mathbf{k} \cdot \mathbf{n}_b \dot{\epsilon}(t) m_b, \quad (12)$$

which differs from the total luminosity (10) by a factor $\mathbf{k} \cdot \mathbf{n}$, representing the angle between the observer and the unit vector in the direction of negative gradient of τ .

The averaged effective temperature presented in Fig. 6 is simply $T_{\text{eff}} = (L/\sigma_{\text{SB}} S_{\text{ph}})^{1/4}$. Here S_{ph} is the surface area of the photosphere, which is computed using the following expansion in terms of SPH quantities:

$$\int_{\Sigma} dS = \sum_b \frac{m_b}{\rho_b} \int_{\Sigma} W_b(\mathbf{r}) dS \quad (13)$$

$$\approx \sum_{b \cap \Sigma} \frac{m_b}{\rho_b} h_b \sigma_b(h_b, \Delta_b/h_b), \quad (14)$$

where $h_b \sigma_b(h_b, \Delta_b/h_b)$ is the contribution from the smoothing kernel of b with the surface integrals replaced by integrals over respective tangent planes. The quantity Δ_b for a particle b is its distance from the integration surface. For the cubic spline kernel that we use (see, e.g. Schoenberg 1946),

$$\sigma_b(h, q) = \frac{1}{h^2} \begin{cases} 0.7 - q^2 + 0.75q^4 - 0.3q^5, & \text{if } q < 1, \\ 0.8 - 2q^2 + 2q^3 & \text{if } 1 \leq q < 2, \\ 0, & \text{if } q \geq 2. \end{cases} \quad (15)$$

The ‘kernel slices’ defined in this manner are normalized such that $2h^2 \int_0^2 \sigma_b(h, q) dq = 1$.

4.3 Results from the 3D remnant matter distribution

We calculate the light curves following the method outlined in the previous section for a sequence of late time (hours and days) distributions of the expanding dynamic ejecta. Here we deal exclusively with dynamic ejecta, while the additional signature from neutrino-driven winds is discussed later in §5. The dynamically ejected mass is around $0.01 M_{\odot}$ and it has typical initial velocities of $0.1\text{--}0.2 c$, see Table 1. As discussed in §3 and in more detail in Paper I, this matter consists of a ‘strong’ r-process material with $A > 130$ and likely has large effective opacities around $\kappa = 10 \text{ cm}^2/\text{g}$ (Kasen et al. 2013; Tanaka & Hotokezaka 2013). We use this value in all our calculations and all results are presented with this opacity. However, the time in the problem scales like $\kappa^{1/2}$

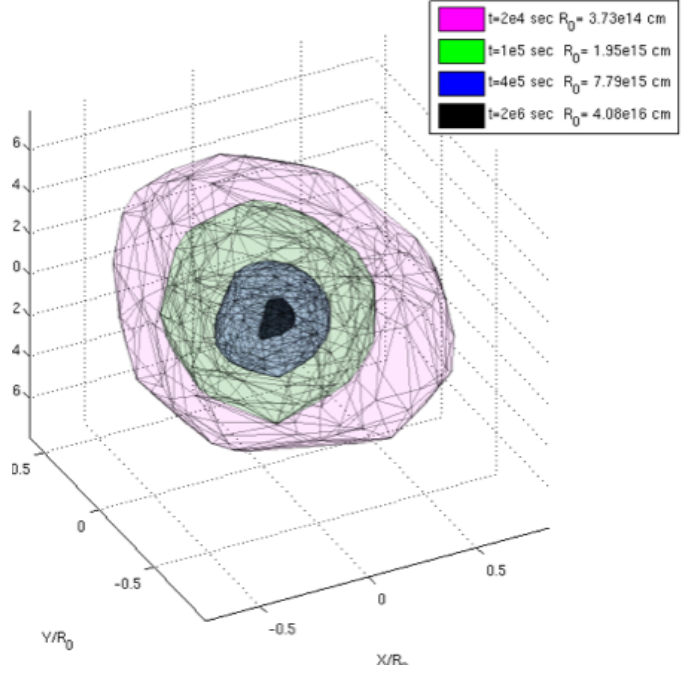


Figure 5. The photospheric surfaces at different moments of time ($2^4, 10^5, 4 \times 10^5$ and 2×10^6 s). The scales are normalized and should be multiplied by 3.73×10^{14} , 1.95×10^{15} , 7.79×10^{15} and 4.08×10^{16} cm, respectively. These surfaces reflect the observed shape of the macronova.

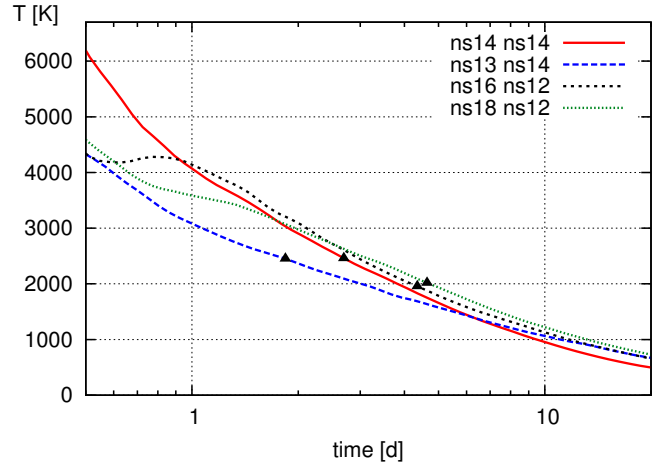


Figure 6. The effective photospheric temperature for the four different merger models. These temperatures should be taken with caution as they do not reflect possible effects of the opacity. The black triangles represent peak times of the bolometric lightcurves.

and the peak luminosity scales like $\kappa^{-\alpha/2}$, see equations (4) and (5). Therefore, the results can be easily rescaled to a configuration with a different grey constant opacity.

The properties of the macronova light curve depend mainly on four factors: the total mass ejected, its composition which determines the opacity, the mass-velocity distribution and the spatial distribution of mass. Fig. 7 depicts the observed bolometric light curve for the $1.3\text{--}1.4 M_{\odot}$ macronova. In this case $0.014 M_{\odot}$ were ejected with a median velocity (after being accelerated by the radioactive decay) of $0.086 c$.

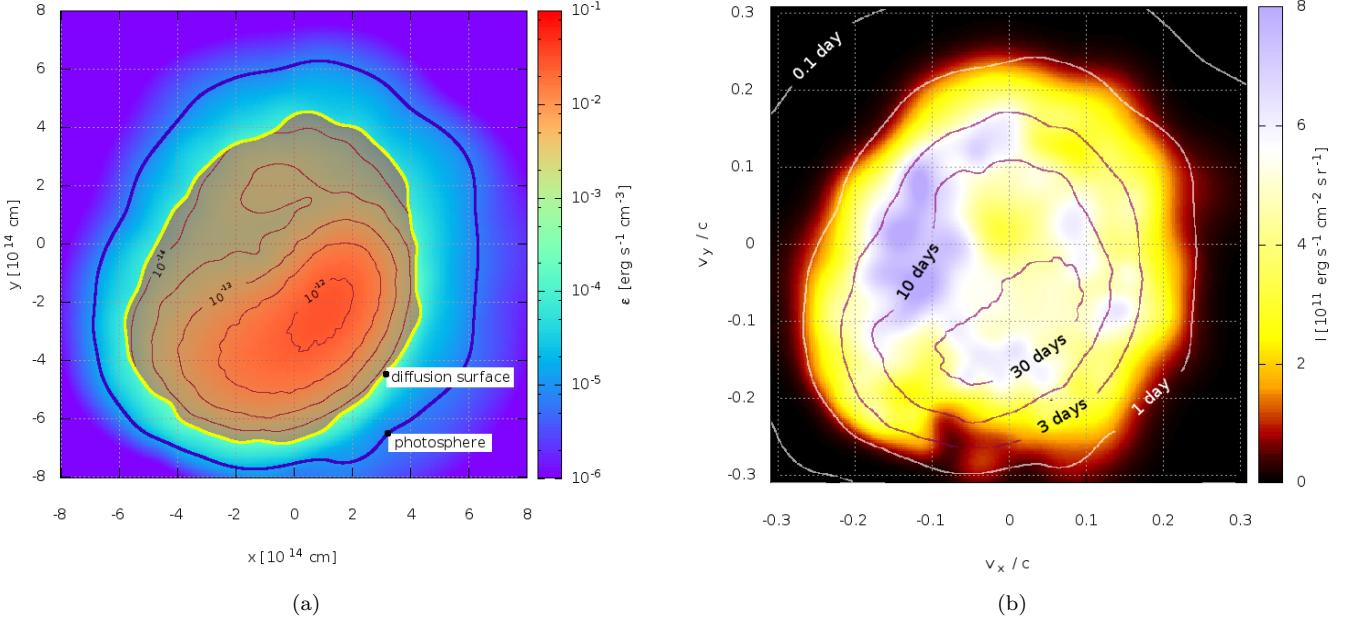


Figure 4. Configuration of the remnant for the merger case $1.3\text{--}1.4 M_{\odot}$ at $t_0 = 1$ d: (a) XY -cut through the density distribution. The thick blue and yellow lines delineate the photosphere and the diffusion surface respectively, and the thin red lines inside the diffusion surface are for five density isocontours, equally spaced (in log scale) from 10^{-14} to 10^{-12} g/cm^3 . Colour-coded is the volume emissivity (nuclear energy generation rate per volume). The blue layer between the diffusion surface and the photosphere is the main contributor to the total luminosity of the remnant. Photons inside the diffusion surface are ‘trapped’ due to high optical depth, while the photons outside photosphere have a very hard spectrum and escape before their energy is converted to visible or infrared. (b) Map of specific intensity, emitted from the photosphere in the z -direction (in the direction of the ‘top’ observer), plotted in velocity space. Visible shape of the photosphere and the column density determine the relative brightness of the transient in a given direction. Superimposed are the cuts of the photosphere in the XY plane at different times, which also coincide with the isocontours of optical depth.

Table 2. Overview of the resulting light curves: the peak time, t_p , peak luminosity L_p , and the effective temperature at the peak. Also shown are the simple estimates (equations 4 and 5) of the peak time, \tilde{t}_p , and the peak luminosity, \tilde{L}_p .

Run ($m_1 - m_2$)	t_p (d)	L_p (erg/s)	T_{eff} (K)	\tilde{t}_p (d)	\tilde{L}_p (erg/s)
A (1.4 – 1.4)	2.7	2.6×10^{40}	2500	5.7	2.7×10^{40}
B (1.3 – 1.4)	1.8	1.7×10^{40}	2500	6.2	2.6×10^{40}
C (1.6 – 1.2)	4.3	4.4×10^{40}	2000	8.1	4.3×10^{40}
D (1.8 – 1.2)	4.6	3.9×10^{40}	2000	8.1	4.3×10^{40}

The simplest order of magnitude estimates (equations 4 and 5) give for $m_{\text{ej}} = 0.014 M_{\odot}$ and $\bar{v} = 0.086 c$ a peak time of $\tilde{t}_p \sim 6 \times 10^5 \text{ s} \sim 7 \text{ d}$ and a peak luminosity of $\tilde{L}_p \sim 10^{41} \text{ erg/s}$. The peak time given by equation (4) is slightly later than the one obtained by the detailed calculations. However, the light curve is very flat and the difference as compared with the simple estimate is moderate. This is consistent with the expectations for a non-spherical system where the photospheric surface is larger, more radiation can leak out and the peak flux is reached earlier. Remarkably, the simple order of magnitude estimate gives an effective temperature of 2200 K, which is very close to the more detailed calculations. A similar comparison of the simple estimates with the detailed calculation shows a similar trend for the other cases (see Table 2).

In Fig. 7, we show the bolometric light curves for four dif-

ferent viewing angles (viewing angles for all models are displayed in Fig. 1). For comparison we show the average 3D bolometric light curve and the light curve calculated for a spherical configuration with the same mass-velocity distribution and the emission from the optically thin region being disregarded. They all show a very broad peak ranging from 1 to 10 d with a maximum at about 2 d. The maximal bolometric luminosity is around $2 \times 10^{40} \text{ erg/s}$ within a factor of 2 for different viewing angles. The peak values of luminosity correspond to absolute magnitudes of -11 to -12.

Fig. 8 depicts the observed bolometric light curves for all cases that we have examined. While the specific shape of the light curves varies somewhat from one case to another, the overall trends remain the same with the emission from the top being typically brighter by about a factor of 2 than the view from the front. For the $1.4\text{--}1.4 M_{\odot}$ case, the peak is narrower, later (at around 2.5-3 d) and brighter with absolute magnitude ranging from -12 to -12.5. For the two remaining cases, $1.6\text{--}1.2 M_{\odot}$ and $1.8\text{--}1.2 M_{\odot}$ the peak is wide, late (at around 4-5 d) and brighter with absolute magnitude ranging from -12.5 to -13.5. In these latter two cases, there is a clear shift of the peak as seen by different observers. Table 2 summarizes the basic results of the different cases. As expected from simple analytic scalings, the cases in which more mass is ejected are more luminous and peak later. Also, the symmetric equal-mass case $1.4\text{--}1.4 M_{\odot}$ exhibits a brighter and later peak compared to the case of $1.3\text{--}1.4 M_{\odot}$ with roughly the same mass. Not too surprisingly, the effective temperatures are rather low.

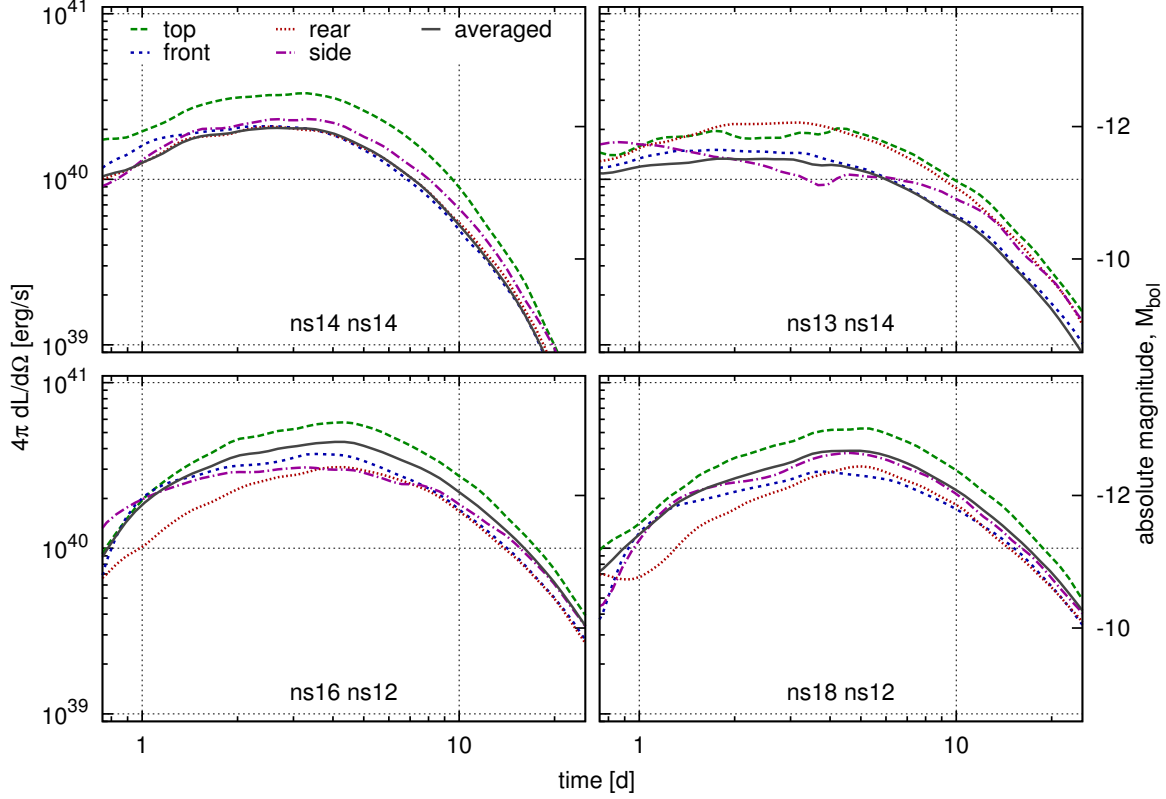


Figure 8. Bolometric equivalents for all four merger models that we have examined, as seen by different observers (oriented as shown in Fig. 1). The black solid line shows the average light curve, which also corresponds to the total power emitted in UV, visible or infrared. The right axis is also labelled according to the corresponding absolute magnitudes.

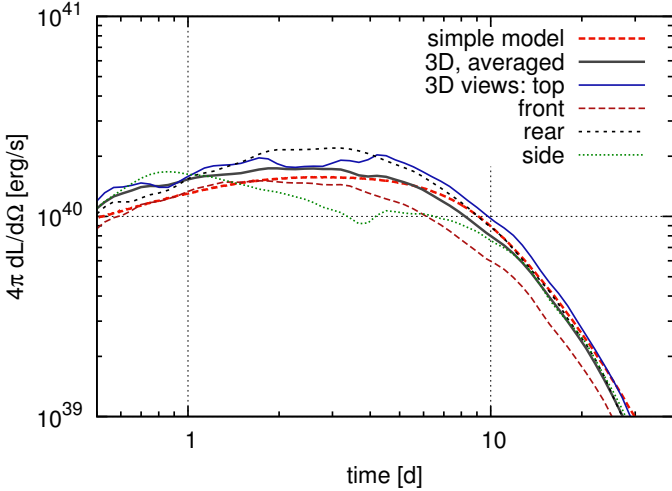


Figure 7. Bolometric equivalents for the 1.3–1.4 M_{\odot} macronova, produced using different models. The thick dashed (red) line corresponds to the simple spherical model without $\tau < 2/3$ region (see § 4.1), calculated using the actual mass-velocity distribution $m(v)$ of the 1.3–1.4 M_{\odot} remnant. Different thin lines show the light curves calculated in 3D for four different observer views (see Fig. 1), and the thick black line represents the averaged light curve, which also equals the total luminosity.

5 NEUTRINO DRIVEN WINDS

The neutrino-driven winds from an ns merger remnant can plausibly complement the nucleosynthesis with ‘weak’ r-process contributions ($50 \lesssim A \lesssim 130$), see section 4.2 of Paper I and they can also plausibly produce an additional EM transient. Barnes & Kasen (2013) discussed observational prospects for winds that are powered by ^{56}Ni . However, as discussed in Paper I, we expect the Y_e values in the wind to lie in a range from 0.28 to 0.40, i.e. they are substantially below the ≈ 0.5 that is needed to synthesize ^{56}Ni . Nevertheless, we find a range of radioactive isotopes with half-lives long enough to power a short-lived transient, as can be seen in Fig.9, bottom row. The top row shows the corresponding nuclear heating rates compared to the heating rates from the dynamical ejecta (dashed blue line on the plots). The larger variation due to individual isotopes, most pronounced in the highest Y_e case, is also apparent in the lightcurves, which could in principle be used for identifying the isotope composition of the winds.

As described in Paper I, our model uses a simple linear expansion profile $\rho(t) = \rho_0(1 + vt/R_0)^{-3}$ and starts from the entropy and Y_e values that are expected from the neutrino properties of our merger cases ($8 k_B/\text{baryon}$; $0.28 \leq Y_e \leq 0.40$). Based on the results of Dessart et al. (2009), their Fig. 2, we select the initial density $\rho_0 = 5 \times 10^7 \text{ g cm}^{-3}$, characteristic radius $R_0 = 200 \text{ km}$ and expansion velocity $v = 0.11c$. We parametrize the unknown wind mass in a range from

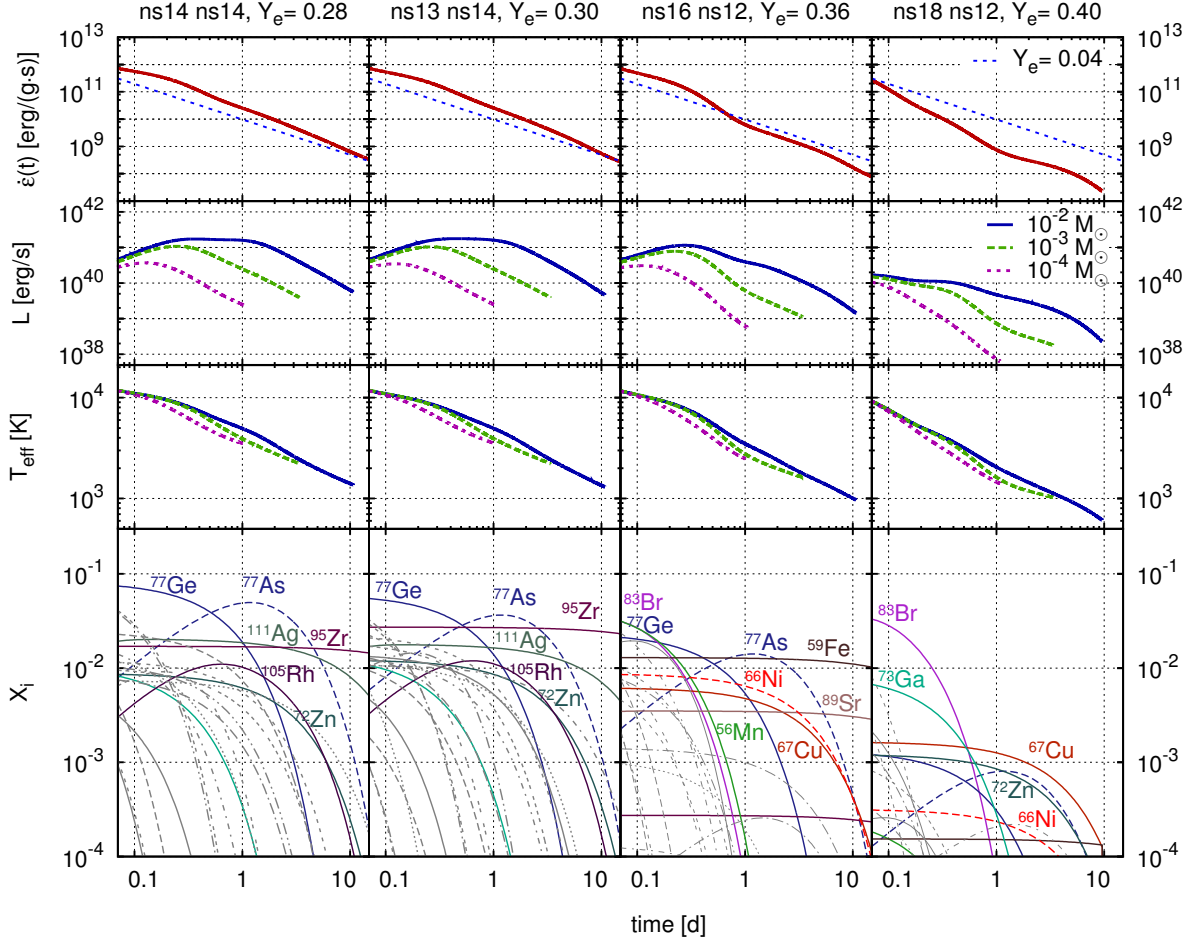


Figure 9. Radioactively powered transients due to neutrino-driven wind. Shown are the radioactive heating rates (first row), light curves (second row) and effective temperatures (third row) for all different runs. Note that these light curves are powered by different material than the ‘macronovae’ from the dynamic ejecta. To highlight this difference, the top row also shows the nuclear heating power from the dynamic ejecta with $Y_e = 0.04$. The bottom row displays the outflow composition in terms of the mass fractions of the dominant radioactive isotopes as a function of time. This material has also different opacities than the macronova material (we assumed $\kappa = 1 \text{ cm}^2/\text{g}$).

10^{-4} to $10^{-2}M_{\odot}$, see the discussion in section 4.2 of Paper I. If the amount of mass ejected by the ν -driven wind is too small, the transient may be obscured from the observer by the previously ejected dynamical component. However, the dynamical ejecta are mainly concentrated around the equatorial plane. This can be seen in Fig. 2b, which shows the fraction of the dynamically ejected mass within the polar angle θ . Less than $10^{-4}M_{\odot}$ is obscuring the inner 30° from the rotation axis, and less than $10^{-3}M_{\odot}$ is within the inner 60° for all our merger simulations. The initial mass distribution is even flatter as can be seen from Fig. 2b.

To calculate the light curves from the radioactive wind material, we apply a simple spherical semianalytic model (as described in Section 4.1) with the radial density profile $\rho(r) = \rho_0(1 - v^2/v_{\text{max}}^2)^3$ with $v_{\text{max}} = 0.35 c$ and the opacity of $\kappa = 1 \text{ cm}^2 \text{ g}^{-1}$. As discussed earlier, such opacities are suitable for a mixture of elements heavier than iron

but much less opaque compared to lanthanides². Because of the low concentration of dynamical ejecta component in the polar regions, we can also ignore possible admixing of lanthanides from the dynamical component.

We feed our model directly with the energy production rate taken from the nucleosynthesis network. We find that the transients caused by neutrino-driven winds can reach up to $1.8 \times 10^{41} \text{ erg/s}$ (for the most optimistic case with $10^{-2}M_{\odot}$) and that they peak after 1 to 12 h in the UV/optical, see Table 3. Like for the case of the dynamic ejecta, we expect that a more detailed treatment would yield shorter times to peak and higher temperatures and luminosities, due to geometric effects related to the photosphere that are not captured in the used semianalytic model. Given the importance of EM signatures of compact binary mergers for GW detections such transients from neutrino-driven winds deserve more detailed studies in future work.

² Our nucleosynthesis calculations indicate the presence of only trace amounts of lanthanides.

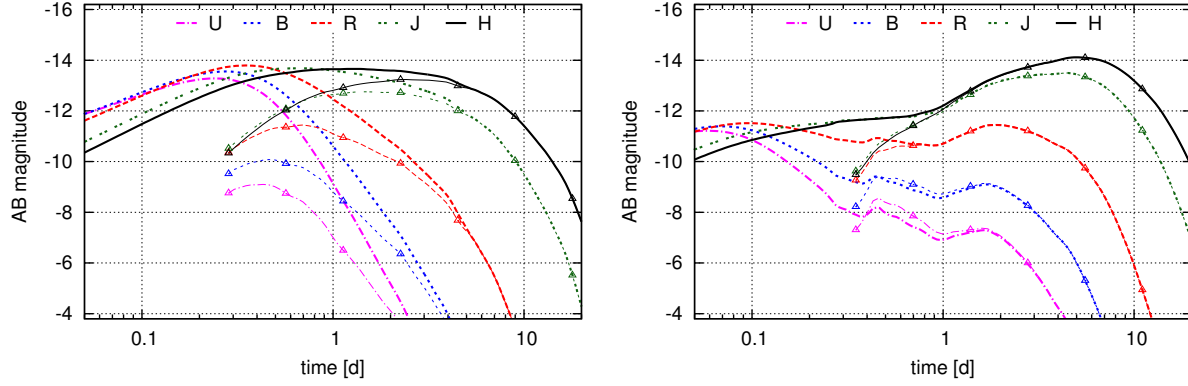


Figure 10. Broad-band light curves from the total ejected material (dynamic ejecta plus ν -driven wind; thick lines) and the dynamically ejected matter alone (symbols). The mass of the ν -driven wind material is set to $10^{-3}M_{\odot}$. The left-hand panel shows the $1.4\text{--}1.3 M_{\odot}$ case, and the right one refers to the $1.8\text{--}1.2 M_{\odot}$ case. As a word of caution we stress that the broad-band light curves have been computed assuming a blackbody spectrum corresponding to the effective temperature.

Table 3. Summary of the results from the neutrino-driven wind model. The mass in the wind is parametrized from 10^{-4} to $10^{-2}M_{\odot}$.

Run ($m_1 - m_2$)	m_{wind} (M_{\odot})	t_{peak} (d)	L_{peak} (erg/s)	T_{eff} (K)
A (1.4 – 1.4)	10^{-2}	0.36	1.7×10^{41}	7700
	10^{-3}	0.25	1.1×10^{41}	8700
	10^{-4}	0.13	3.7×10^{40}	9900
B (1.3 – 1.4)	10^{-2}	0.46	1.8×10^{41}	7000
	10^{-3}	0.27	1.0×10^{41}	8500
	10^{-4}	0.13	3.5×10^{40}	9800
C (1.6 – 1.2)	10^{-2}	0.27	1.1×10^{40}	7800
	10^{-3}	0.22	7.8×10^{40}	8400
	10^{-4}	0.11	3.1×10^{40}	10000
D (1.8 – 1.2)	10^{-2}	0.07	1.7×10^{40}	9500
	10^{-3}	0.06	1.5×10^{40}	9800
	10^{-4}	0.05	1.2×10^{40}	10700

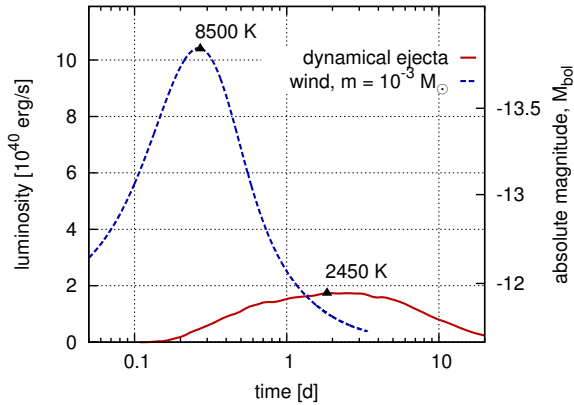


Figure 11. Combined light curves for the $1.3 - 1.4 M_{\odot}$ configuration from the dynamically ejected material and the neutrino-driven wind.

6 DETECTABILITY

Before turning to examine the detectability of the calculated light curves we note that our IR light curves from the dynamical ejecta, are dimmer than those of Kasen et al. (2013) and of Tanaka & Hotokezaka (2013). As mentioned in §3 both groups have used radioactive heating rates that on few days are larger by a factor of 3-4 than our radioactive heating rate (see fig. 5 of Paper I). We suspect that this is mainly due to the use of fixed, too large values for the initial electron fraction. Once we correct for the effect from the energy generation, our results are in reasonable agreement with Barnes & Kasen (2013). It is worth stressing once more, though, that they use a more elaborate radiative transfer model (but based on a less sophisticated model for the matter distribution). In particular, our conclusions are based on effective temperatures and therefore there is still room for an enhancement of the IR part of the spectrum that might enhance the emission in this part of the spectrum. Overall, our estimates of the IR emission from the dynamical ejecta are two magnitudes dimmer than those of Kasen et al. (2013) and of Tanaka & Hotokezaka (2013), which would make the detectability of these signals an extremely challenging endeavour.

The most important question concerning these transients is whether they can be used to identify ns mergers. Or, put differently, are the macronova signals detectable? When addressing this question two kinds of search modes need to be considered: a follow-up search after a GW trigger or a detection in a blind search. In the first case, the GW trigger provides an error box of $\sim 100 \text{ deg}^2$. Given the importance of the discovery, one can expect that significant resources would be allocated for this task. Blind transient searches are routine now [e.g. Palomar Transient Factory (PTF) and Panoramic Survey Telescope & Rapid Response System (Pan-STARRS)] at modest magnitudes. Deeper or high cadence optical searches will continue at accelerated pace with various telescopes [e.g. Zwicky Transient Factory (ZTF)] and will culminate with the operation of the LSST (LSST Science Collaborations et al. 2009). SASIR (Bloom et al. 2009) is the only planned transit search in the IR.

We turn now to examine the detectability of macronovae in these two modes.

We begin by a quick summary of the expected signals. Table 4 describes the expected signals for the 1.4–1.3 and 1.8–1.2 M_{\odot} cases. These are the weakest and strongest signals and other configurations or signals from preferred directions can be stronger by about a factor of 2 (corresponding to about one magnitude). Fig. 10 shows the broad-band light curves for these two cases, calculated assuming that radiation is emitted with a blackbody spectrum filtered with the standard filter functions for the *UBVRI* (Bessell & Murphy 2012) and *JHK* (Cohen et al. 2003) bands. Before turning to these results we stress once more that temperatures estimated here are just effective temperatures and should be taken as such. It may very well be that the real signal would be non-thermal and heavily dominated by unknown details of the opacity, radiation transfer and photon emission processes. This can modify significantly the detectability estimates presented here.

The first source is the main IR signal from the dynamical ejecta. It peaks around 3–6 d after the ns² merger, with a peak absolute magnitude of (-12.8, . . . , -13.9). The temperature at this time is about 2300–1800 K and most of the emissions will be radiated in the *J–H* band (1.26 ± 0.1 , $1.65 \pm 0.13 \mu\text{m}$). Initially, the temperatures of this component are higher than 4000 K for about half a day, see Fig. 6. This early signal from the dynamically ejected outflow would be in the visible, provided that no line blanketing occurs. It is relatively weak (-11.6, . . . , -10.8), thus it is of no surprise that it would be hard to detect. Another source is the emission from the ν -driven winds (see Fig. 11). The emission from the ν -driven winds has an absolute magnitude of (-11.2, . . . , -13.7), depending on the poorly known total mass ejected. Although it is short lived (0.4–0.8 d), its high temperature (8000 K) and high luminosity make it a more prominent signal and its detection much easier. We consider two possible ν wind cases, $0.01M_{\odot}$ and of $10^{-3}M_{\odot}$, respectively. These signals seem to be the strongest among the three considered, but they are about one and a half magnitudes weaker than the previous estimates for macronovae signals that were based on a lower opacity of $\kappa = 0.1\text{cm}^2/\text{g}$ (e.g. Metzger et al. 2010; Goriely et al. 2011; Roberts et al. 2011; Metzger & Berger 2012; Bauswein et al. 2013; Piran et al. 2013).

Table 5 summarizes the characteristics of a few relevant detectors. VISTA (Emerson et al. 2006) is the largest wide field IR telescope operating today. With its 4 m mirror it can reach 21.5 mag in a 100 s exposure. In the optical, Subaru is the largest wide-field telescope available; with Hyper-suprime camera it would easily reach 25th mag over a field of view (FoV) of $\approx 1.5 \text{ deg}^2$, and it is most suitable for a follow-up survey. Pan-STARRS (Kaiser et al. 2002) is an active transient survey with a limiting magnitude of 24.6 and a FoV of 3 deg^2 . Zwicky Transient Factory (ZTF) that will replace the PTF is a planned shallow survey ($\approx 21 \text{ mag}$) with a huge FoV (of the order of 30 deg^2). The ultimate LSST (LSST Science Collaborations et al. 2009) with a FoV of 9.6 deg^2 , will reach a typical limiting magnitude of 24.

Turning now to detectability, we find that the observations are challenging. A follow-up detection requires covering of a 100 deg^2 region at an $\approx 24 - 25 \text{ mag}$ in the IR for the main

Table 5. A few telescopes that can search for these transients. The magnitude given is for a 5σ detection and for an exposure time of $t_{\text{exp}} = 100 \text{ s}$. One can go deeper with the detection magnitude satisfying roughly $m_{\text{lim}}(t) \approx m_{\text{lim}}(t_0) - 2.5 \log[(t/t_0)^{1/2}]$.

Telescope	Band	$M_I(\text{AB})$ For $t_{\text{exp}} = 100 \text{ s}$	FoV (deg^2)
VISTA	<i>J</i>	21.5	2.2
SASIR	<i>J</i>	23	0.2-1.7
Subaru (Hyper-suprime camera)*	<i>B</i>	25	1.5
LSST	<i>r</i>	25.3	9.6
	<i>i</i>	24.6	
ZTP	-	21.6	30
Pan-STARRS	<i>i</i>	24.6	3

* We use the Hypersuprime camera FoV with sensitivity estimated from the suprimecam parameters. The Hypersuprime camera sensitivity might be slightly better.

– ZFT filters are undecided as yet.

signal from the dynamic ejecta³, at $\approx 25 - 26 \text{ mag}$ for the initial optical signal from the dynamic and at $23 - 24 \text{ mag}$ for the ν -wind signal. From those, the first main signal in the IR is impossible to detect. The optical signals are feasible, but require some effort. One can cover, for example, the whole 100 deg^2 using the Subaru Hypersuprime camera at 25th B mag within an hour. Thus one can obtain even two coverings of the region looking for rapid variability. Alternatively one can cover this region by multiple rapid observations of ZFT reaching within one night a 24th magnitude. Once such a source is found, a follow-up at $\approx 24 - 25 \text{ mag}$ at IR is extremely challenging from Earth (this might be possible with a several hours exposure on VISTA, but doable from space). Such a combined strategy seems to be optimal. The flat light curve lasting a few days could allow some time for this IR observation.

With these magnitudes, detection in blind surveys seems hopeless. Even with the LSST, one could expect only a few detections per year (assuming an event rate of $300/\text{yr}/\text{Gpc}^3$). These will be single-event detections, and unless rapidly identified (from this single observation) and followed up by further optical and IR observations, it will be impossible to confirm. Without much more detailed information on the spectral and to some extent temporal characteristics of these transients, it would be an impossible task to identify suitable candidates within the huge number of transients expected in the LSST.

7 SUMMARY AND DISCUSSION

In this set of two papers we have investigated the long-term evolution of ns merger remnants. In the companion paper

³ A more sophisticated search can cover only a fraction of this area focusing on regions with nearby galaxies (e.g. Metzger et al. 2013). We do not discuss the details of this strategy here.

Table 4. Parameters of the transients, associated with dynamical ejecta and ν -driven winds, for two extreme cases: 1.3–1.4 M_{\odot} and 1.8–1.2 M_{\odot} . M_p is the absolute AB magnitude in the relevant band of the detector, m_p is the magnitude at 300 Mpc, t_p is the time since merger, and T_p is the estimated effective temperature at this time. The last column lists horizon distances for the 5- σ detection with the exposure of 100 s.

Source ($m_1 - m_2$)	M_p (AB) / Band	t_p (d)	T_p (K)	m_p (AB) (@ 300 Mpc)	Horizon (Mpc) / Inst (@ 100 s).
Dynamical ejecta:					
1.4–1.3 M_{\odot} , Main phase	-12.8 / <i>J</i>	2	2300	24.6	72 / VISTA 144 / SASIR
1.8–1.2 M_{\odot} , Main phase	-13.9 / <i>H</i>	6	1860	23.4	95 / VISTA 208 / SASIR
1.4–1.3 M_{\odot} , Initial phase	-11.6 / <i>i</i>	0.6	4000	25.8	174 / LSST and Pan-STARRS
1.8–1.2 M_{\odot} , Initial phase	-10.8 / <i>i</i>	0.7	4000	26.6	120 / LSST and Pan-STARRS
ν -driven winds:					
1.4–1.3 M_{\odot} , $m_{\text{ej}} = 10^{-2} M_{\odot}$	-14.3 / <i>r</i> -14.6 / <i>B</i>	0.8	7676	23.0 23.3	847 / LSST 650 / HSC [†]
1.8–1.2 M_{\odot} , $m_{\text{ej}} = 10^{-2} M_{\odot}$	-11.5 / <i>r</i> -11.5 / <i>B</i>	<0.3	9480	25.8 25.8	231 / LSST 201 / HSC [†]
1.4–1.3 M_{\odot} , $m_{\text{ej}} = 10^{-3} M_{\odot}$	-13.7 / <i>r</i> -13.5 / <i>B</i>	0.4	8740	23.7 23.8	620 / LSST 516 / HSC [†]
1.8–1.2 M_{\odot} , $m_{\text{ej}} = 10^{-3} M_{\odot}$	-11.3 / <i>r</i> -11.4 / <i>B</i>	<0.3	9800	26.0 26.0	213 / LSST 188 / HSC [†]

[†] The Hypersuprime camera (HSC) on the Subaru telescope.

(Rosswog et al. 2013), Paper I, we have followed the long-term evolution of the ejected matter for up to 100 years after the merger. We paid particular attention to the role that the heating from radioactively decaying r-process nuclei plays. We found that the matter that is dynamically ejected (by tidal and/or hydrodynamic interaction) undergoes a ‘strong’ r-process producing a robust pattern of nuclei with $A > 130$. Although the nuclear energy input does alter dynamics and morphology it does not erase the memory of the initial binary mass ratio. We have further calculated in a simple model the nucleosynthesis for the expected neutrino-driven wind. We find that also this wind undergoes an r-process, though a ‘weak’ one which produces abundance distributions in the range $50 \lesssim A \lesssim 130$ that vary substantially between different merger cases. This is because the neutrino luminosities in the different cases yield different Y_e values within the wind ($0.28 \lesssim Y_e \lesssim 0.40$) and the nucleosynthesis is in this parameter range rather sensitive to the exact value of the electron fraction.

Here we have explored in some detail the properties of radioactively powered transients from both dynamic ejecta and neutrino-driven winds. All calculations of the macronova light curves for dynamic ejecta that have been performed so far have assumed that the expansion is homologous. In Paper I, this assumption is dropped and we have explicitly followed the long-term evolution of the dynamical ejecta including radioactive heating. The ejecta composition within the dynamic ejecta is unique and very different from any type of supernova. Supernovae produce elements up to the iron group near $Z = 26$, but the dynamic ejecta of ns mergers consist entirely of r-process elements up to the third peak near $Z \approx 90$ and should thus produce unique features in the EM signal. As recently argued based on atomic struc-

ture calculations by Kasen et al. (2013), this material has orders of magnitudes larger opacities than the iron-group-like values that have been used in previous work. The recent work by Kasen et al. (2013) and Tanaka & Hotokezaka (2013) favours values around $10 \text{ cm}^2/\text{g}$ and this is the value that we have adopted in the current study. Overall, these higher opacities lead to later, weaker and redder emission in comparison to earlier macronova models, but calculations based on the true matter distribution are substantially brighter, peak earlier and at higher effective temperatures than the corresponding models of Li & Paczyński (1998). This is because the latter assume a uniform matter distribution and therefore cannot capture geometric and dynamic properties of the radiating volume. We identify this volume as the location between a diffusion surface (where the diffusion time equals the dynamical time) and the photospheric surface with $\tau = 2/3$. In addition, there is a radiation component from the optically thin region with $\tau < 2/3$. These photons are produced by radioactive decays and escape with a spectrum that is unknown to us.

Using the nucleosynthesis results from our simple neutrino-driven wind model we also estimate the light curves of the corresponding EM transients that arise from this component of the outflow. According to our estimates these winds should have electron fractions substantially below 0.5 and therefore they do not produce any ^{56}Ni . Still they produce radioactive long-lived enough isotopes that lead to radioactive transients. These isotopes have a substantially lower opacity, as compared with the opacity of the dynamically ejected outflow. The resulting transients peak, therefore, at very early times (< 0.5 d) and are substantially brighter and hotter than the transients produced by the dynamic ejecta (see Tab. 3). Their ν -wind transients are relatively

bright ($\sim 10^{41}$ erg/s) with effective temperatures from 5000 to 10000 K and they proceed the redder and longer lived dynamical ejecta transients. It is worth stressing, however, that the amount of mass in these winds is not well known and we have parametrized it here with values ranging from 10^{-4} to $10^{-2} M_{\odot}$. The actual signal depends, of course, on this mass.

The prospects for unambiguous detection, however, seem not very optimistic. For the numbers we consider most plausible, the detection prospects for the dynamic ejecta transients seem dim, even the more promising signals from the neutrino-driven winds seem one and a half magnitudes lower than previous dynamic ejecta predictions based on the iron-group-like opacities. Both signals are too dim to be identified in blind searches. Such searches are carried out in the optical and as such the ν -driven wind component is the only one having a chance of being detected. However, with reasonable estimates of the merger event rate even the mammoth LSST will detect only a few such transients per year and with a single detection these are most likely to be lost within millions of other transients discovered. The situation is somewhat better with a GW trigger. Such a trigger will provide an ~ 100 deg² error box. Even with this information, a search for the IR signal from the dynamical ejecta is impossible with current technology. *WFIRST* (Spergel et al. 2013) is the only mission that could possibly perform such a search, but it is far from clear that it will ever be launched. Under optimistic conditions the transient from a significant ($10^{-2} M_{\odot}$) ν -driven wind can then be possibly detected, for example using the Hypersuprime camera on Subaru, in a dedicated follow-up search that will cover the whole error box with a sufficient depth. With some luck this UV/optical can be detected even using a continuous exposure of a smaller telescope (like the ZFT) that has a very wide FoV. Once such a transient is detected and localized an IR follow-up is possible. This will require quick allocation of a significant amount of time on the best IR facilities available, but the stakes are high. A combined detection of both signals would provide a ‘smoking gun’ signature confirming the nature of the transient as an ns merger-driven macronova.

Tanvir et al. (2013) and Berger et al. (2013) discovered recently, using the *Hubble Space Telescope*, an nIR transient at the location of the short burst GRB 130603B. This transient had an apparent magnitude of 25.3 ± 0.3 corresponding to $M_{J,AB} \approx -15.35$ approximately seven days after the burst in the progenitor rest frame. Both groups suggest that, while not fully conclusive, this could have been a macronova signature of a merger event. The observed magnitude is consistent with the models of Barnes & Kasen (2013); Tanaka & Hotokezaka (2013) and Hotokezaka et al. (2013). However, as mentioned earlier (§3), we believe that the nuclear heating rate used in these models and hence the observed flux at the crucial time is overestimated by a factor of 3 – 4 and as our average estimates are 2 mag below this observed transient. On the other hand, as the GRB was observed, it is natural to assume that the system had a favourable orientation (the ‘top’ view). This would enhance the luminosity by a factor of 2 relative to the average one. Our estimated signal would still fall short by about 1 mag compared with

the observations⁴. While this difference is within what we consider a reasonable uncertainty of our estimates, significantly more massive dynamical ejecta, as would have been the case in a dynamic nsbh collision (Lee et al. 2010; Rosswog et al. 2013), some nsbh mergers (Rosswog 2005; Deaton et al. 2013; Foucart et al. 2013; Hotokezaka et al. 2013; Kyutoku et al. 2013; Lovelace et al. 2013; Tanaka et al. 2014) or a higher Y_e (which could arise in a disruption of a particularly small ns with a large crust) could possibly bridge this gap.

ACKNOWLEDGEMENTS

We would like to thank C. Winteler for providing his nucleosynthesis network code and for his continued support and for helpful comments. This work has also benefited from the stimulating discussions at the MICRA workshop in 2013. We gratefully acknowledge helpful discussions with Mattias Ergon, Claes Fransson, Ariel Goobar, Ehud Nakar, Dovi Poznanski, Jesper Sollerman and Ivan Zalamea. DG and TP were supported by an ERC advanced grant (GRBs) and by the I-CORE Programme of the Planning and Budgeting Committee and The Israel Science Foundation (grant no. 1829/12). SR and OK were supported by DFG grant RO-3399, AOBJ-584282 and by the Swedish Research Council (VR) under grant 621-2012-4870. SR has been supported by Compstar. The simulations of this paper were performed on the facilities of the Höchstleistungsrechenzentrum Nord (HLRN).

REFERENCES

- Abadie J. et al., 2010, CQG, 27, 173001, ADS
- Accadia T. et al., 2011, CQG, 28, 114002, ADS
- Aloy M. A., Janka H.-T., Müller E., 2005, A&A, 436, 273, ADS
- Arun K. G. et al., 2009, CQG, 26, 094027, ADS
- Barnes J., Kasen D., 2013, ApJ, 775, 18, ADS
- Bartos I., Brady P., Márka S., 2013, CQG, 30, 123001, ADS
- Bauswein A., Goriely S., Janka H.-T., 2013, ApJ, 773, 78, ADS
- Beloborodov A. M., 2008, in M. Axelsson ed., AIPConf. Ser. Vol. 1054, Hyper-accreting Black Holes. pp 51–70, ADS
- Berger E., 2009, ApJ, 690, 231, ADS
- Berger E., 2010, ApJ, 722, 1946, ADS
- Berger E., Fong W., Chornock R., 2013, ApJ, 774, L23, ADS
- Bessell M., Murphy S., 2012, PASP, 124, 140, ADS
- Bloom J. S. et al. 2009, preprint (arXiv:0902.1527)
- Bloom J. S. et al. 2009, preprint (arXiv:0905.1965)
- Caballero O. L., McLaughlin G. C., Surman R., 2012, ApJ, 745, 170, ADS

⁴ Additionally, the material from dissolution of the accretion disc (not considered here) will have higher $Y_e \sim 0.2$ and correspondingly higher nuclear energy release at late times (see fig.6 of Paper I). If the amount of mass ejected in this channel is comparable to the dynamically ejected mass, this can affect our detectability estimates.

- Cohen M., Wheaton W. A., Megeath S. T., 2003, *AJ*, 126, 1090, ADS
- Coward D. M. et al. 2012, *MNRAS*, 425, 2668, ADS
- Dalal N., Holz D. E., Hughes S. A., Jain B., 2006, *Phys. Rev. D*, 74, 063006, ADS
- Deaton M. B. et al. 2013, *ApJ*, 776, 47, ADS
- Dessart L., Ott C. D., Burrows A., Rosswog S., Livne E., 2009, *ApJ*, 690, 1681, ADS
- Eichler D., Livio M., Piran T., Schramm D. N., 1989, *Nature*, 340, 126, ADS
- Emerson J., McPherson A., Sutherland W., 2006, *The Messenger*, 126, 41, ADS
- Fernández R., Metzger B. D., 2013, *MNRAS*, 435, 502, ADS
- Fong W., Berger E., Fox D. B., 2010, *ApJ*, 708, 9, ADS
- Fong W. et al. 2012, *ApJ*, 756, 189, ADS
- Fong W. et al. 2013, *ApJ*, 769, 56, ADS
- Foucart F. et al. 2013, *Phys. Rev. D*, 87, 084006, ADS
- Freiburghaus C., Rosswog S., Thielemann F.-K., 1999, *ApJ*, 525, L121, ADS
- Goriely S., Bauswein A., Janka H.-T., 2011, *ApJL*, 738, L32, ADS
- Guetta D., Piran T., 2006, *A&A*, 453, 823, ADS
- Guetta D., Stella L., 2009, *A&A*, 498, 329, ADS
- Harry G. M. et al. 2010, *CQG*, 27, 084006, ADS
- Hoffman R. D., Woosley S. E., Qian Y.-Z., 1997, *ApJ*, 482, 951, ADS
- Hotokezaka K., Kiuchi K., Kyutoku K., Okawa H., Sekiguchi Y., Shibata M., Taniguchi K., 2013, *Phys. Rev. D*, 87, 024001, ADS
- Hotokezaka K., Kyutoku K., Tanaka M., Kiuchi K., Sekiguchi Y., Shibata M., Wanajo S., 2013, *ApJ*, 778, L16, ADS
- Hughes S. A., Holz D. E., 2003, *CQG*, 20, 65, ADS
- Kaiser N. et al. 2002, in J. A. Tyson & S. Wolff ed., *Proc. SPIE Conf. Ser.* 4836, Pan-STARRS: A Large Synoptic Survey Telescope Array. p 154, ADS
- Kalogera V. et al. 2004b, *ApJ*, 614, L137, ADS
- Kalogera V. et al. 2004a, *ApJ*, 601, L179, ADS
- Kasen D., Badnell N. R., Barnes J., 2013, *ApJ*, 774, 25, ADS
- Kasliwal M. M., Nissanke S., 2013, preprint (arXiv:1309.1554),
- Kelley L. Z., Mandel I., Ramirez-Ruiz E., 2012, *Physical Review D*, 87, 17, ADS
- Kochanek C. S., Piran T., 1993, *ApJL*, 417, L17, ADS
- Korobkin O., Rosswog S., Arcones A., Winteler C., 2012, *MNRAS*, 426, 1940, ADS
- Kulkarni S. R., 2005, preprint (arXiv:astro-ph/0510256),
- Kupka F. G., Ryabchikova T. A., Piskunov N. E., Stempels H. C., Weiss W. W., 2000, *Baltic Astronomy*, 9, 590, ADS
- Kyutoku K., Ioka K., Shibata M., 2013, *Phys. Rev. D*, 88, 041503, ADS
- Lattimer J. M., Mackie F., Ravenhall D. G., Schramm D. N., 1977, *ApJ*, 213, 225, ADS
- Lattimer J. M., Schramm D. N., 1974, *ApJ*, 192, L145, ADS
- Lee W. H., Ramirez-Ruiz E., 2007, *New Journal of Physics*, 9, 17, ADS
- Lee W. H., Ramirez-Ruiz E., López-Cámara D., 2009, *ApJL*, 699, L93, ADS
- Lee W. H., Ramirez-Ruiz E., van de Ven G., 2010, *ApJ*, 720, 953, ADS
- Li L., Paczyński B., 1998, *ApJL*, 507, L59, ADS
- Lovelace G., Duez M. D., Foucart F., Kidder L. E., Pfeiffer H. P., Scheel M. A., Szilágyi B., 2013, *CQG*, 30, 135004, ADS
- LSST Science Collaborations et al., 2009, preprint (arXiv:0912.0201),
- Metzger B. D., Berger E., 2012, *ApJ*, 746, 48, ADS
- Metzger B. D., Kaplan D. L., Berger E., 2013, *ApJ*, 764, 149, ADS
- Metzger B. D. et al. 2010, *MNRAS*, 406, 2650, ADS
- Metzger B. D., Piro A. L., Quataert E., 2008, *MNRAS*, 390, 781, ADS
- Metzger B. D., Piro A. L., Quataert E., 2009, *MNRAS*, 396, 304, ADS
- Monaghan J. J., 2005, *Reports on Progress in Physics*, 68, 1703, ADS
- Nakar E., 2007, *Phys. Rep.*, 442, 166, ADS
- Nakar E., Gal-Yam A., Fox D. B., 2006, *ApJ*, 650, 281, ADS
- Nakar E., Piran T., 2011, *Nature*, 478, 82, ADS
- Narayan R., Piran T., Shemi A., 1991, *ApJ*, 379, L17, ADS
- Nissanke S., Kasliwal M., Georgieva A., 2013, *ApJ*, 767, 124, ADS
- Phinney E. S., 1991, *ApJ*, 380, L17, ADS
- Phinney E. S., 2009, in *Astro2010: The Astronomy and Astrophysics Decadal Survey*, Vol. 2010, Finding and Using Electromagnetic Counterparts of Gravitational Wave Sources. p 235, ADS
- Piran T., 2004, *Reviews of Modern Physics*, 76, 1143, ADS
- Piran T., Nakar E., Rosswog S., 2013, *MNRAS*, 430, 2121, ADS
- Qian Y.-Z., Woosley S. E., 1996, *ApJ*, 471, 331, ADS
- Roberts L. F., Kasen D., Lee W. H., Ramirez-Ruiz E., 2011, *ApJL*, 736, L21+, ADS
- Rosswog S., 2005, *ApJ*, 634, 1202, ADS
- Rosswog S., 2009, *New Astronomy Reviews*, 53, 78, ADS
- Rosswog S., 2013, *Philosophical Transactions A*, 1210.6549, ADS
- Rosswog S., Davies M. B., 2002, *MNRAS*, 334, 481, ADS
- Rosswog S., Davies M. B., Thielemann F.-K., Piran T., 2000, *A&A*, 360, 171, ADS
- Rosswog S., Korobkin O., Arcones A., Thielemann F.-K., Piran T., 2013,
- Rosswog S., Liebendörfer M., 2003, *MNRAS*, 342, 673, ADS
- Rosswog S., Liebendörfer M., Thielemann F.-K., Davies M., Benz W., Piran T., 1998, in Mezzacappa A., ed., *Proc. 2nd Oak Ridge Symp., Atomic and Nuclear Astrophysics, Mass ejection in neutron star mergers.* p 729, ADS
- Rosswog S., Liebendörfer M., Thielemann F.-K., Davies M. B., Benz W., Piran T., 1999, *A&A*, 341, 499, ADS
- Rosswog S., Piran T., Nakar E., 2013, *MNRAS*, 430, 2585, ADS
- Rosswog S., Price D., 2007, *MNRAS*, 379, 915, ADS
- Rosswog S., Ramirez-Ruiz E., 2002, *MNRAS*, 336, L7, ADS
- Rosswog S., Ramirez-Ruiz E., 2003, *MNRAS*, 343, L36, ADS
- Rosswog S., Ramirez-Ruiz E., Davies M. B., 2003, *MNRAS*, 345, 1077, ADS
- Rosswog S., Ramirez-Ruiz E., Hix W. R., Dan M., 2008, *Computer Physics Communications*, 179, 184, ADS

- Rowlinson A., et al., 2010, MNRAS, p. 1479, ADS
Ruffert M., Janka H., Takahashi K., Schaefer G., 1997, A & A, 319, 122, ADS
Schoenberg I. J., 1946, Quart. Appl. Math., 4, 45
Shen H., Toki H., Oyamatsu K., Sumiyoshi K., 1998a, Nuclear Physics A, 637, 435, ADS
Shen H., Toki H., Oyamatsu K., Sumiyoshi K., 1998b, Progress of Theoretical Physics, 100, 1013, ADS
Somiya K., 2012, CQG, 29, 124007, ADS
Spergel D. et al. 2013, preprint (arXiv:1305.5425)
Springel V., 2010, ARAA, 48, 391, ADS
Surman R., McLaughlin G. C., Ruffert M., Janka H., Hix W. R., 2008, ApJL, 679, L117, ADS
Tanaka M., Hotokezaka K., 2013, ApJ, 775, 113, ADS
Tanaka M., Hotokezaka K., Kyutoku K., Wanaajo S., Kiuchi K., Sekiguchi Y., Shibata M., 2014, ApJ, 780, 31, ADS
Tanvir N. R., Levan A. J., Fruchter A. S., Hjorth J., Hounsell R. A., Wiersema K., Tunnicliffe R. L., 2013, Nature, 500, 547, ADS
Thielemann F.-K. et al. 2011, Progress in Particle and Nuclear Physics, 66, 346, ADS
Timmes F. X., Swesty F. D., 2000, ApJS, 126, 501, ADS
Wanaajo S., Janka H.-T., 2012, ApJ, 746, 180, ADS
Winteler C., 2012, PhD thesis, University Basel, CH, edoc
Winteler C., Käppeli R., Perego A., Arcones A., Vasset N., Nishimura N., Liebendörfer M., Thielemann F.-K., 2012, ApJL, 750, L22, ADS

This paper has been typeset from a \TeX / \LaTeX file prepared by the author.